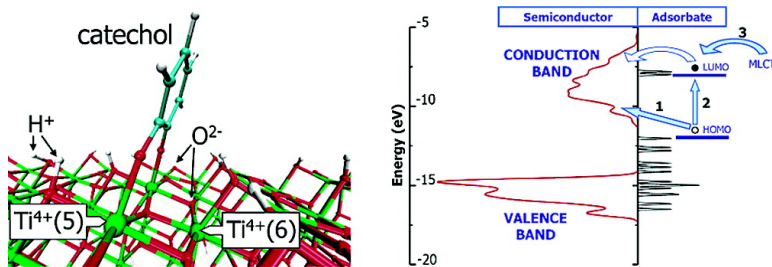


## Influence of Thermal Fluctuations on Interfacial Electron Transfer in Functionalized TiO Semiconductors

Sabas G. Abuabara, Luis G. C. Rego, and Victor S. Batista

*J. Am. Chem. Soc.*, **2005**, 127 (51), 18234-18242 • DOI: 10.1021/ja055185u • Publication Date (Web): 02 December 2005

Downloaded from <http://pubs.acs.org> on March 25, 2009



### More About This Article

Additional resources and features associated with this article are available within the HTML version:

- Supporting Information
- Links to the 12 articles that cite this article, as of the time of this article download
- Access to high resolution figures
- Links to articles and content related to this article
- Copyright permission to reproduce figures and/or text from this article

[View the Full Text HTML](#)

## Influence of Thermal Fluctuations on Interfacial Electron Transfer in Functionalized TiO<sub>2</sub> Semiconductors

Sabas G. Abuabara,<sup>†</sup> Luis G. C. Rego,<sup>‡</sup> and Victor S. Batista<sup>\*†</sup>

Contribution from the Department of Chemistry, Yale University, P.O. Box 208107, New Haven, Connecticut 06520-8107, and Department of Physics, Universidade Federal de Santa Catarina, Florianopolis, SC 88040-900, Brazil

Received August 15, 2005; E-mail: victor.batista@yale.edu

**Abstract:** The influence of thermal fluctuations on the dynamics of interfacial electron transfer in sensitized TiO<sub>2</sub>-anatase semiconductors is investigated by combining ab initio DFT molecular dynamics simulations and quantum dynamics propagation of transient electronic excitations. It is shown that thermal nuclear fluctuations speed up the underlying interfacial electron transfer dynamics by introducing nonadiabatic transitions between electron acceptor states, localized in the vicinity of the photoexcited adsorbate, and delocalized states extended throughout the semiconductor material, creating additional relaxation pathways for carrier diffusion. Furthermore, it is shown that room-temperature thermal fluctuations reduce the anisotropic character of charge diffusion along different directions in the anatase crystal and make similar the rates for electron injection from adsorbate states of different character. The reported results are particularly relevant to the understanding of temperature effects on surface charge separation mechanisms in molecular-based photo-optic devices.

### 1. Introduction

Interfacial electron transfer in semiconductor materials plays a central role in a variety of photoinduced reactions in electrochemistry,<sup>1–5</sup> photocatalysis,<sup>6,7</sup> imaging,<sup>8</sup> as well as in practical applications to photo-optic devices for solar energy conversion cells<sup>9–12</sup> and artificial photosynthesis.<sup>13</sup> The elementary reaction step involves electron transfer from an adsorbate molecule into the semiconductor host substrate, a process that remains poorly understood despite significant research effort reported in recent years, including experimental,<sup>14–29</sup> com-

putational,<sup>30–45</sup> and theoretical<sup>46–53</sup> studies. In particular, the influence of thermal fluctuations on the underlying electron

<sup>†</sup> Yale University.

<sup>‡</sup> Universidade Federal de Santa Catarina.

- (1) Miller, R. J. D.; McLendon, G.; Nozik, A. J.; Schimickler, W.; Willig, F. *Surface Electron-Transfer Processes*; VCH: New York, 1995.
- (2) Hagfeldt, A.; Grätzel, M. *Chem. Rev.* **1995**, *95*, 49–68.
- (3) Nozik, A. J.; Memming, R. *J. Phys. Chem.* **1996**, *100*, 13061–13078.
- (4) Kamat, P.; Meisel, D., Eds. *Semiconductor Nanoclusters - Physical, Chemical and Catalytic Aspects; Studies in Surface Science and Catalysis 103*; Elsevier: Amsterdam, 1997.
- (5) Anderson, N. A.; Lian, T. Q. *Annu. Rev. Phys. Chem.* **2005**, *56*, 491–519.
- (6) Zhao, W.; Ma, W. H.; Chen, C. C.; Zhao, J. C.; Shuai, Z. G. *J. Am. Chem. Soc.* **2004**, *126*, 4782–4783.
- (7) Huang, W. Y.; Yu, Y. *Prog. Chem.* **2005**, *17*, 242–247.
- (8) Jacobson, K.; Jacobson, R. E. *Imaging Systems: Mechanisms and Applications of Established and New Photosensitive Processes*; John Wiley & Sons: New York, 1976.
- (9) O'Regan, B.; Grätzel, M. *Nature* **1991**, *353*, 737–740.
- (10) Grätzel, M. *Nature* **2001**, *414*, 338–344.
- (11) Hagfeldt, A.; Grätzel, M. *Acc. Chem. Res.* **2000**, *33*, 269–277.
- (12) Moser, J. E.; Bonnôte, P.; Grätzel, M. *Coord. Chem. Rev.* **1998**, *171*, 245–250.
- (13) Fujishima, A.; Honda, K. *Nature* **1972**, *238*, 37–38.
- (14) Asbury, J. B.; Ellingson, R. J.; Ghosh, H. N.; Ferrere, S.; Nozik, A. J.; Lian, T. Q. *J. Phys. Chem. B* **1999**, *103*, 3110–3119.
- (15) Asbury, J. B.; Hao, E.; Wang, Y. Q.; Ghosh, H. N.; Lian, T. Q. *J. Phys. Chem. B* **2001**, *105*, 4545–4557.
- (16) Asbury, J. B.; Anderson, N. A.; Hao, E.; Ai, X.; Lian, T. Q. *J. Phys. Chem. B* **2003**, *107*, 7376–7386.
- (17) Anderson, N. A.; Ai, X.; Lian, T. Q. *J. Phys. Chem. B* **2003**, *107*, 14414–14421.
- (18) Bauer, C.; Boschloo, G.; Mukhtar, E.; A., H. *Int. J. Photoenergy* **2002**, *1*, 17–20.
- (19) Huber, R.; Moser, J.-E.; Grätzel, M.; Wachtveitl, J. *J. Phys. Chem. B* **2002**, *106*, 6494–6499.
- (20) Schnadt, J.; Brühwiler, P. A.; Patthey, L.; O'Shea, J. N.; Södergren, S.; Odelius, M.; Ahuja, R.; Karis, O.; Bäessler, M.; Persson, P.; Siegbahn, H.; Lunell, S.; Mårtensson, N. *Nature* **2002**, *418*, 620–623.
- (21) Schnadt, J.; O'Shea, J. N.; Patthey, L.; Kjeldgaard, L.; Åhlund, J.; Nilson, K.; Schiessling, J.; Krempaský J.; Shi, M.; Karis, O.; Glover, C.; Siegbahn, H.; Mårtensson, N.; Brühwiler, P. A. *J. Chem. Phys.* **2003**, *119*, 12462–12472.
- (22) Schnadt, J.; Henningsson, A.; Andersson, M. P.; Karlsson, P. G.; Uvdal, P.; Siegbahn, H.; Brühwiler, P. A.; Sandell, A. *J. Phys. Chem. B* **2004**, *108*, 3114–3122.
- (23) Willig, F.; Zimmermann, C.; Ramakrishna, S.; Storck, W. *Electrochem. Acta* **2000**, *45*, 4565–4575.
- (24) Zimmermann, C.; Willig, F.; Ramakrishna, S.; Burfeindt, B.; Pettinger, B.; Eichberger, R.; Storck, W. *J. Phys. Chem. B* **2001**, *105*, 9245–9253.
- (25) Hannappel, T.; Burfeindt, B.; Storck, W.; Willig, F. *J. Phys. Chem. B* **1997**, *101*, 6799–6802.
- (26) Ramakrishna, G.; Singh, A. K.; Palit, D. K.; Ghosh, H. N. *J. Phys. Chem. B* **2004**, *108*, 1701–1707.
- (27) Ramakrishna, G.; Singh, A. K.; Palit, D. K.; Ghosh, H. N. *J. Phys. Chem. B* **2004**, *108*, 4775–4783.
- (28) Ramakrishna, G.; Singh, A. K.; Palit, D. K.; Ghosh, H. N. *J. Phys. Chem. B* **2004**, *108*, 12489–12496.
- (29) Moser, J.; Punchedewa, S.; Infelta, P. P.; Grätzel, M. *Langmuir* **1991**, *7*, 3012–3018.
- (30) Persson, P.; Lunell, S.; Ojamäe L. *Chem. Lett.* **2002**, *364*, 469–474.
- (31) Persson, P.; Bergstrom, R.; Lunell, S. *J. Phys. Chem. B* **2000**, *104*, 10348–10351.
- (32) Persson, P.; Lundqvist, M. *J. Phys. Chem. B* **2005**, *109*, 11918–11924.
- (33) Duncan, W. R.; Stier, W. M.; Prezhdo, O. V. *J. Am. Chem. Soc.* **2005**, *127*, 7941–7951.
- (34) Duncan, W. R.; Prezhdo, O. V. *J. Phys. Chem. B* **2005**, *109*, 365–373.
- (35) Smith, B. B.; Nozik, A. J. *J. Phys. Chem. B* **1999**, *103*, 9915–9932.
- (36) Smith, B. B.; Nozik, A. J. *Chem. Phys.* **1996**, *205*, 47–72.
- (37) Stier, W.; Prezhdo, O. V. *J. Mol. Struct. (THEOCHEM)* **2003**, *630*, 33–43.
- (38) Stier, W.; Prezhdo, O. V. *J. Phys. Chem. B* **2002**, *106*, 8047–8054.
- (39) Stier, W.; Duncan, W. R.; Prezhdo, O. V. *Adv. Mater.* **2004**, *16*, 240–244.
- (40) Thoss, M.; Kondov, I.; Wang, H. B. *Chem. Phys.* **2004**, *304*, 169–181.
- (41) Rego, L. G. C.; Batista, V. S. *J. Am. Chem. Soc.* **2003**, *125*, 7989–7997.

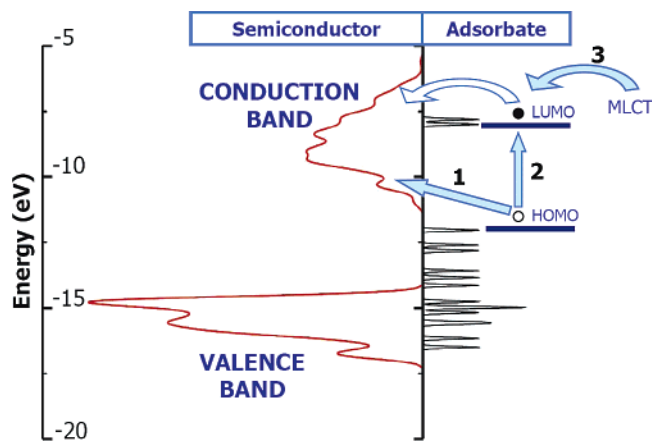


**Figure 1.** Density of states of TiO<sub>2</sub>-anatase functionalized with catechol. The diagram shows the energy level of the adsorbate surface complex, the TiO<sub>2</sub> valence and conduction bands, and a schematic representation of three possible injection processes: direct adsorbate–substrate charge transfer excitation (arrow 1); vertical photoexcitation process (arrow 2) and subsequent electron injection into the conduction band of the host material (curved arrow); and population of the LUMO as part of a MLCT state (arrow 3).

injection time scale and relaxation mechanism has yet to be understood at the quantitative level.<sup>17,21,22,37–39,47</sup> This paper addresses the effect of thermal nuclear motion on the interfacial electron transfer dynamics in TiO<sub>2</sub>-anatase semiconductors functionalized with catechol, an aromatic linker of great interest,<sup>54–56</sup> which has been the subject of experimental<sup>29,57–60</sup> and theoretical<sup>34,41–43</sup> studies.

TiO<sub>2</sub>-anatase is an inexpensive, nontoxic, and photostable semiconductor material. However, its wide band gap (~3.2 eV) limits the efficiency of the native semiconductor in direct applications to solar energy phototransduction devices, a limitation commonly overcome by surface sensitization. Surface complexes, formed upon adsorption of organic or inorganic molecules, often introduce additional electronic states within the semiconductor band gap (see energy diagram in Figure 1). Such states sensitize the host material for photoabsorption at

lower frequencies, leading to photoinduced interfacial electron transfer when there is a suitable energy match between the photoexcited state and the manifold of electronic states in the conduction band of the semiconductor. The efficiency of photon-to-current conversion thus relies upon optimal conditions for the underlying electron transfer mechanism as well as on the rational design of dyes and linker photosensitizers.

Catechol has raised significant experimental interest as a prototype of an aromatic linker upon which a wide range of molecular structures can be attached for specific functionalities, including applications to photovoltaic devices with high incident photon-to-current conversion efficiencies.<sup>54–56</sup> As a model sensitizer, catechol lowers the TiO<sub>2</sub> absorption threshold from 370 to 600 nm, with a shoulder peaking around 420 nm due to a direct charge transfer excitation from the catechol HOMO to the conduction band<sup>29,31,34,44,45,58–60</sup> (see arrow 1 in Figure 1).

“Vertical” transitions to higher-energy electronic states of the surface complexes are also allowed transitions<sup>31,34,60</sup> and correspond closely to the catechol HOMO–LUMO and HOMO–(LUMO+1) states (see arrow 2 in Figure 1). As pointed out by Grätzel, Nozik, Lian, and others,<sup>2,14,15,28,55</sup> efficient photoinjection mechanisms from larger organometallic dye molecules involve reaction pathways via these higher electronic states of the aromatic linker (i.e., metal-to-ligand charge transfer states (MLCTs) involving the  $\pi^*$  levels; see arrow 3 in Figure 1). Thus in focusing on photoinjection mechanisms from the excited electronic states of catechol (arrows 2 and 3), this paper examines the process of electron injection through catechol in its likely application to the design of an efficient phototransductive device. In particular, this work addresses the influence of thermal nuclear motion on the time scales and mechanisms of interfacial electron transfer, complementing previous studies of catechol/TiO<sub>2</sub>-anatase semiconductors<sup>41–43</sup> and recent theoretical and experimental work addressing the nature of interfacial electron transfer in other functionalized semiconductor materials.<sup>17,21,22,28,33,37–39</sup> However, the reported results are expected to stimulate the development of femtosecond-pulse spectroscopic measurements that might directly probe the electron injection dynamics from the native excited states of catechol (arrow 2), even in the presence of competing direct catechol–TiO<sub>2</sub> charge transfer excitations (arrow 1) and possibly stronger (depending on substrate surface coverage) semiconductor band-to-band transitions.

Interfacial electron transfer in functionalized semiconductors is typically completed within the subpicosecond time scale, as reported for various different systems.<sup>5,19,20,22,25,26</sup> Reaction times as short as a few femtoseconds have also been reported for systems, such as TiO<sub>2</sub> functionalized with (bi)-isonicotinic acid,<sup>20,21</sup> alizarin,<sup>19,33</sup> and catechol.<sup>41</sup> There is also substantial experimental evidence that the primary electron transfer event in dye-sensitized semiconductors occurs much faster than vibrational relaxation of the photoexcited chromophore,<sup>17,22–24,27</sup> suggesting electron injection mechanisms driven by electronic coupling rather than by nuclear reorganizational motion.<sup>16,17,20,22,46</sup> The quantitative description of interfacial electron injection thus seems to be beyond the capabilities of the traditional electron transfer theories, based on weak coupling schemes, where electron transfer rates are determined by the time scale of nuclear reorganizational motion.<sup>61–63</sup> Theoretical extensions to the

- (42) Rego, L. G. C.; Abuabara, S. G.; Batista, V. S. *J. Chem. Phys.* **2005**, *122*, 154709 (1–6).  
 (43) Rego, L. G. C.; Abuabara, S. G.; Batista, V. S. *Quantum Info. Comput.* **2005**, *5*, 318–334.  
 (44) Redfern, P. C.; Zapol, P.; Curtiss, L. A.; Rajh, T.; Thurnauer, M. C. *J. Phys. Chem. B* **2003**, *107*, 11419–11427.  
 (45) De Angelis, F.; Tilocca, A.; Selloni, A. *J. Am. Chem. Soc.* **2004**, *126*, 15024–15025.  
 (46) Ramakrishna, S.; Willig, F. *J. Phys. Chem. B* **2000**, *104*, 68–77.  
 (47) Ramakrishna, S.; Willig, F.; May, V. *J. Chem. Phys.* **2001**, *115*, 2743–2756.  
 (48) Boroda, Y. G.; Voth, G. A. *J. Chem. Phys.* **1996**, *104*, 6168–6183.  
 (49) Boroda, Y. G.; Calhoun, A.; Voth, G. A. *J. Chem. Phys.* **1997**, *107*, 8940–8954.  
 (50) Kornyshev, A. A.; Schmickler, W. *J. Electroanal. Chem.* **1985**, *185*, 253–261.  
 (51) Petersson, A.; Ratner, M.; Karlsson, H. O. *J. Phys. Chem. B* **2000**, *104*, 8498–8502.  
 (52) Gao, Y. Q.; Georgievskii, Y.; Marcus, R. A. *J. Chem. Phys.* **2000**, *112*, 3358–3369.  
 (53) Gao, Y. Q.; Marcus, R. A. *J. Chem. Phys.* **2000**, *113*, 6351–6360.  
 (54) Rice, C. R.; Ward, M. D.; Nazeeruddin, M. K.; Grätzel, M. *New J. Chem.* **2000**, *24*, 651–652.  
 (55) Mosurkal, R.; He, J.-A.; Yang, K.; Samuelson, L. A.; Kumar, J. *J. Photochem. Photobiol. A* **2004**, *168*, 191–196.  
 (56) Galoppini, E. *Coord. Chem. Rev.* **2004**, *248*, 1283–1297.  
 (57) Gerhards, M.; Perl, W.; Schumm, S.; Henrichs, U.; Jacoby, C.; Kleiner-manns, K. *J. Chem. Phys.* **1996**, *104*, 9362–9375.  
 (58) Rodriguez, R.; Blesa, M. A.; Regazzoni, A. E. *J. Colloid Interface Sci.* **1996**, *177*, 122–131.  
 (59) Liu, Y.; Dadap, J. I.; Zimdars, D.; Eisenthal, K. B. *J. Phys. Chem. B* **1999**, *103*, 2480–2486.  
 (60) Wang, Y. H.; Hang, K.; Anderson, N. A.; Lian, T. Q. *J. Phys. Chem. B* **2003**, *107*, 9434–9440.

(61) Newton, M. D. *Chem. Rev.* **1991**, *91*, 767–792.

strong electronic coupling (adiabatic) limit, typically based on the Anderson–Newns Hamiltonian, have been developed and applied to the description of metal electrodes and semiconductor/liquid interfaces.<sup>46–50</sup> While these models have provided valuable insight, applications to electron transfer in dye-sensitized semiconductor nanostructures rely upon simplifying assumptions with regards to the description of the electronic structure and coupling model.<sup>23,24,40</sup> Ideally, however, one would like to implement more rigorous theoretical descriptions facing the challenge of modeling both the electronic structure and the nuclear relaxation explicitly in terms of fully atomistic simulations of the underlying electron transfer dynamics.

Previous computational studies of interfacial electron transfer in catechol/TiO<sub>2</sub>-anatase nanostructures were focused on the analysis of ultrafast interfacial electron transfer under vacuum and cryogenic temperature conditions.<sup>41</sup> These studies found that the primary charge separation event is completed in  $\tau \approx 6$  fs, even when there is negligible participation of thermal nuclear fluctuations at cryogenic temperature. The ultrafast charge separation process is followed by an anisotropic delocalization of the injected charge throughout the nanostructure, a diffusional process that can be up to an order of magnitude slower along the  $[-101]$  direction than along the  $[010]$  or the  $[101]$  crystallographic directions in the anatase crystal. Furthermore, the overall electron injection rates were found to be strongly dependent on the character of the initially populated electronic state of the adsorbate molecule since the nodal planes of the native catechol molecular orbitals determine their respective coupling strengths with host substrate states and, consequently, the nature of the electron injection reaction path.<sup>41</sup>

The main focus of this paper is to address the influence of room-temperature nuclear fluctuations on the electron injection dynamics in catechol/TiO<sub>2</sub>-anatase semiconductors, with emphasis on the potential effect of nuclear motion on both the reaction rates and electron injection mechanisms found earlier at lower temperature.<sup>41</sup> The reported simulations show that room-temperature thermal fluctuations create new pathways for electron relaxation at the sensitized semiconductor interface. The resulting effect is a net speed-up of electron injection and a manifestly isotropic diffusion of the injected charge along the semiconductor host substrate.

The implemented methodology adopts a mixed quantum-classical approach based on Ehrenfest dynamics, with a classical description of the nuclear motion evolving on an effective mean field potential. Electronic degrees of freedom are described by a time-dependent extended Hückel Hamiltonian,<sup>42</sup> which is particularly suited to investigate nonadiabatic dynamics in a dense manifold of electronic states, providing insight on the role that electronic state symmetry and chemical bonding play in the underlying relaxation mechanism.<sup>41</sup> Conditions under which quantum relaxation dynamics can be approximated by such quantum-classical treatments have been investigated for many years.<sup>37,38,42,43,64–75</sup> In particular, quantum coherences have

been studied in similar composite models where a quantum subsystem (electronic state) is coupled to a buffer subsystem (nuclear coordinates) which is directly coupled to a thermal bath. It has been shown that the applicability of these mixed quantum-classical approaches, where the buffer subsystem is treated classically, is valid so long as the quantum subsystem decoheres slowly and the buffer quickly.<sup>75</sup> In the catechol/anatase system studied here, it is found that the most relevant degrees of freedom to the underlying electronic relaxation are those of the ionic coordinates in the semiconductor crystal. In contrast to vibrational states of the adsorbate chromophore, which may be prepared in coherent superposition states, the ionic degrees of freedom are presumed to be initially at equilibrium with a thermal bath and possess no particular phase relation, that is, a classical approximation for their dynamics is valid.

The paper is organized as follows. The Methods section (section 2) describes the preparation of the catechol/TiO<sub>2</sub>-anatase model system and the computational methodology. Details of the molecular dynamics simulations are discussed in section 2.1. A description of the electronic Hamiltonian is included in section 2.2. Section 2.3. describes the simulations of electronic injection. Results are presented in sections 3.1. and 3.2. A discussion of the results is presented in section 3.3. Finally, section 4 summarizes and concludes.

## 2. Methods

**2.1. Computational Model.** This section outlines only briefly the methodology and the models implemented for the present study of functionalized TiO<sub>2</sub> nanostructures. A more thorough description of the model, including details concerning the ab initio Molecular Dynamics (MD) simulations and the analysis of structural and electronic properties of the models, can be found in previous work.<sup>41–43</sup>

The unit cell model system is composed of 32 [TiO<sub>2</sub>] units arranged according to the anatase crystalline structure,<sup>76</sup> where the (101) surface of the crystal is functionalized with catechol (see Figure 2). The surface dangling bonds are saturated with hydrogen capping atoms in order to quench the formation of surface states,<sup>77</sup> avoiding unphysical low coordination numbers. Periodic boundary conditions are imposed with a vacuum spacer between slabs, making negligible the interaction between distinct surfaces in the infinitely periodic model system. Geometry relaxation as well as thermalization and equilibration under conditions of room temperature and constant volume are performed by using the Vienna ab initio Simulation Package (VASP/VAMP).<sup>78,79</sup> The resulting structural relaxation next to the adsorbate describes the underlying surface reconstruction due to functionalization,<sup>41,80</sup> a process that is partially responsible for quenching the formation of surface states deep within the semiconductor band gap.<sup>77</sup>

The VASP/VAMP package implements the Density Functional Theory (DFT) in a plane wave basis set, making use of the Perdew–Wang<sup>81</sup> generalized gradient approximation for the exchange–correlation

- (62) Barbara, P. F.; Meyer, T. J.; Ratner, M. A. *J. Phys. Chem.* **1996**, *100*, 13148–13168.  
(63) Marcus, R. A.; Sutin, N. *Biochim. Biophys. Acta* **1985**, *811*, 265–322.  
(64) Joos, E.; Zeh, H. D.; Kiefer, C.; Giulini, D.; Kupsch, J.; Stamatescu, I.-O. *Decoherence and the Appearance of a Classical World in Quantum Theory*; Springer-Verlag: Berlin, Heidelberg, 1996.  
(65) Tully, J. C.; Preston, R. K. *J. Chem. Phys.* **1971**, *55*, 562–572.  
(66) Tully, J. C. *J. Chem. Phys.* **1990**, *93*, 1061–1071.  
(67) Hammes-Schiffer, S.; Tully, J. C. *J. Chem. Phys.* **1994**, *101*, 4657–4667.  
(68) Hammes-Schiffer, S.; Tully, J. C. *J. Chem. Phys.* **1995**, *103*, 8528–8537.

- (69) Bittner, E. R.; Rossky, P. J. *J. Chem. Phys.* **1995**, *103*, 8130–8143.  
(70) Prezhdo, O. V.; Rossky, P. J. *Phys. Rev. Lett.* **1998**, *81*, 5294–5297.  
(71) Coker, D. F.; Xiao, L. *J. Chem. Phys.* **1995**, *102*, 496–510.  
(72) Batista, V. S.; Coker, D. F. *J. Chem. Phys.* **1996**, *105*, 4033–4054.  
(73) Batista, V. S.; Coker, D. F. *J. Chem. Phys.* **1997**, *106*, 7102–7116.  
(74) Elola, M. D.; Estrin, D. A.; Laria, D. *J. Phys. Chem. A* **1999**, *103*, 5105–5112.  
(75) Shiokawa, K.; Kapral, R. *J. Chem. Phys.* **2002**, *117*, 7852–7863.  
(76) Vittadini, A.; Selloni, A.; Rotzinger, F. P.; Grätzel, M. *J. Phys. Chem. B* **2000**, *104*, 1300–1306.  
(77) Monch, W. *Semiconductor Surfaces and Interfaces*; Springer Series in Surface Sciences Springer: Berlin, 1993; Vol. 26.  
(78) Kresse, G.; Furthmüller, J. *Phys. Rev. B* **1996**, *54*, 11169–11186 (<http://cms.mpi.univie.ac.at/vasp/>).  
(79) Kresse, G.; Furthmüller, J. *Comp. Mat. Sci.* **1996**, *6*, 15–50.  
(80) Diebold, U. *Surf. Sci. Rep.* **2003**, *48*, 53–229.  
(81) Perdew, J. P. In *Electronic Structure of Solids 91*; Ziesche, P., Eschrig, H., Eds.; Akademie Verlag: Berlin, 1991.



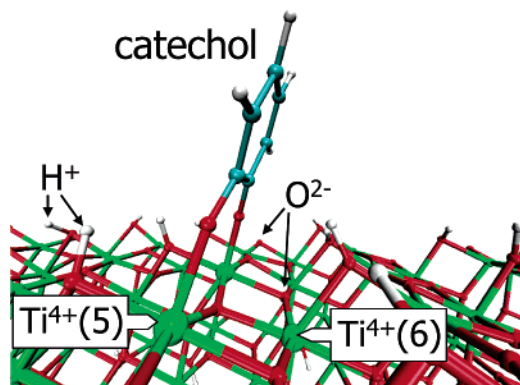


**Figure 2.** Local geometry of the relaxed nanostructure next to the catechol adsorbate. The four types of atoms included in this simulation (Ti, O, C, H) are represented by the colors green, red, turquoise, and white, respectively. The capping hydrogen ions and oxygen ions of the semiconductor lattice are indicated, as is the hexacoordinated Ti<sup>4+</sup> ion near the adsorbate, and the nearest of the two pentacoordinated Ti<sup>4+</sup> ions directly anchoring the catechol adsorbate.

functional (PW91) and ultrasoft Vanderbilt pseudopotentials for modeling the core electrons.<sup>82,83</sup> The Kohn–Sham (KS) Hamiltonian is projected onto a plane-wave basis set, and high-efficiency iterative methods are used to obtain the KS eigenstates and eigenvalues. Self-consistency is accelerated by means of efficient charge density mixing schemes. Thermal configurations and nuclear trajectories of ab initio MD simulations are computed by taking full advantage of the parallelized version of the code with a parallel SP2 supercomputer.

The phonon spectral density, obtained as the Fourier transform of the ionic velocity autocorrelation function, is consistent with previous calculations<sup>41</sup> as well as with the experimentally determined normal modes of the TiO<sub>2</sub>-anatase semiconductor in the 262–876 cm<sup>-1</sup> range.<sup>84</sup> Higher-frequency resonances of the combined catechol–semiconductor crystal complex are mostly localized in the 800–1600 cm<sup>-1</sup> range, the highest (at 3100 cm<sup>-1</sup>) corresponding to the C–H stretching modes of the adsorbed catechol. Most relevant for the study of interfacial electron transfer is the low-frequency portion of the phonon spectrum, which is assigned to vibrational modes of the adsorbate in good agreement with earlier studies of the isolated catechol molecule.<sup>57</sup> These earlier ab initio studies also found that the ground state vibrational frequencies of the catechol molecule are only slightly affected by photoexcitation of the molecule to the S1 electronic state.<sup>57</sup> Further, the delocalized vibrational modes of TiO<sub>2</sub>-anatase are expected to be only marginally affected by photoexcitation of the adsorbate molecule or electron injection into the conduction band (i.e., same vibrational frequencies). Therefore, it is reasonable to assume that nuclear motion is quite insensitive to changes of distinct electronic character during the ultrafast interfacial electron transfer, an approximation successfully applied in previous studies of functionalized semiconductors.<sup>33,42</sup>

**2.2. Electronic Structure.** Realistic simulations of interfacial electronic relaxation face the challenge of modeling quantum dynamics in rather extended model systems since finite size effects or even periodic boundary conditions can produce inaccurate results due to artificial recurrences of electronic population.<sup>41</sup> To address these challenges, electronic relaxation is simulated in 3 nm particles constructed by the juxtaposition of three of the complex units described in section 2.1., extended along the [−101] and [010] crystallographic directions of the TiO<sub>2</sub>-anatase structure (see Figure 3). Periodic boundary conditions are applied along the unextended crystallographic direction in each case.

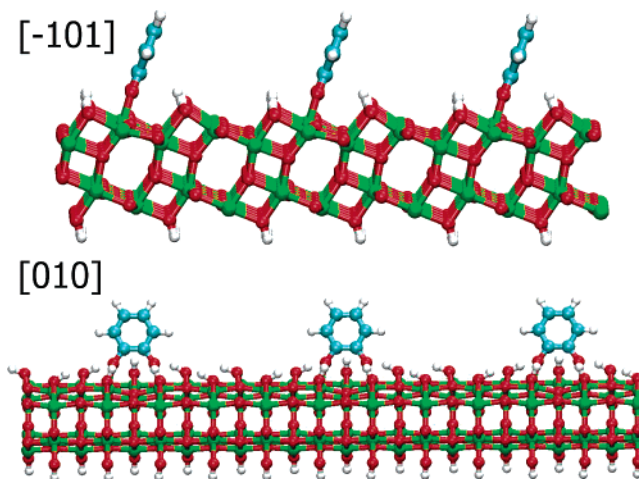


**Figure 3.** TiO<sub>2</sub>-anatase nanostructures extended along the [−101] (upper structure) and [010] directions (lower structure).

The electronic structure of these extended 3 nm particles can be described according to a tight binding model Hamiltonian gained from the extended Hückel (EH) approach.<sup>85,86</sup> Advantages of this method are that it requires a relatively small number of transferable parameters and is capable of providing accurate results for the energy bands of elemental materials (including transition metals) as well as compound bulk materials in various phases.<sup>86</sup> In addition, the EH method is applicable to large extended systems and provides valuable insight on the role of chemical bonding.<sup>87</sup> It is therefore most suitable to develop a clear chemical picture of the underlying relaxation dynamics at the semiquantitative level, in an effort to provide fundamental insight on the role played by initial electronic state spatial distribution and symmetry under conditions of inhomogeneous broadening in the underlying injection mechanism.

The EH Hamiltonian is computed in the basis of Slater-type orbitals  $\chi$  for the radial part of the atomic orbital (AO) wave functions,<sup>41,88</sup> including the 4s, 4p, and 3d atomic orbitals of Ti<sup>4+</sup> ions, the 2s and 2p atomic orbitals of O<sup>2-</sup> ions, the 2s and 2p atomic orbitals of C atoms, and the 1s atomic orbitals of H atoms. The AOs  $\{\chi_i(t)\}$  form a mobile (nonorthogonal) basis set due to nuclear motion, with  $S_{ij}(t) = \langle \chi_i(t) | \chi_j(t) \rangle$ , the corresponding time-dependent overlap matrix elements. The overlap matrix is computed using periodic boundary conditions along the [010] or [−101] directions for the [−101] and [010] extended systems, respectively. Diagonalization of the EH Hamiltonian predicts a 3.3 eV band gap for the 3.0 nm model system in its relaxed configuration (see energy diagram in Figure 1). Considering that the semiconductor band gap is larger for smaller nanoparticles, the 3.3 eV band gap is consistent with the experimental band gap of 3.2 eV for bulk TiO<sub>2</sub>-anatase, 3.4 eV for 2.4 nm particles,<sup>89</sup> and 3.7 eV for the 1.2 nm model system.<sup>41,90</sup>

**2.3. Simulations of Electron Injection.** We confine ourselves to an approximate mixed quantum-classical method in which the electrons are treated quantum mechanically and the nuclei classically. The nuclei evolve on an effective mean-field Potential Energy Surface (PES),  $V_{\text{eff}}$ , according to classical trajectories  $\mathbf{R}^{\xi} = \mathbf{R}^{\xi}(t)$ , with initial conditions specified by index  $\xi$ . The actual calculation of  $V_{\text{eff}}$ , or equivalently of the set of trajectories  $\mathbf{R}^{\xi}(t)$ , is a difficult problem.<sup>91</sup> However, in the

(82) Vanderbilt, D. *Phys. Rev. B* **1990**, *41*, 7892–7895.

(83) Laasonen, K.; Pasquarello, A.; Car, R.; Lee, C.; Vanderbilt, D. *Phys. Rev. B* **1993**, *47*, 10142–10153.

(84) Gonzalez, R. J.; Zallen, R.; Berger, H. *Phys. Rev. B* **1997**, *55*, 7014–7017.

(85) McGlynn, S. P.; Vanquickenborne, L. G.; Kinoshita, M.; Carroll, D. G. *Introduction to Applied Quantum Chemistry*; Holt, Rinehart, and Winston Inc.: New York, 1972.

(86) Cerdá, J.; Soria, F. *Phys. Rev. B* **2000**, *61*, 7965–7971.

(87) Hoffmann, R. *Rev. Mod. Phys.* **1988**, *60*, 601–628.

(88) For a numerical implementation of the method: Landrum, G. A.; Glassy, W. V. The YAeHMOP project, <http://yaehmop.sourceforge.net>.

(89) Hoffmann, M. R.; Martin, S. T.; Choi, W.; Bahnemann, D. W. *Chem. Rev.* **1995**, *95*, 69–96.

(90) Bredow, T.; Geudtner, G.; Jug, K. J. *Chem. Phys.* **1996**, *105*, 6395–6400.

(91) Pechukas, P. *Phys. Rev.* **1969**, *181*, 166–174.

present application, both the ground and excited electronic PESs involve bound nuclear motion of similar frequencies. Therefore,  $V_{\text{eff}}$  is nearly parallel to the ground state PES, and nuclear trajectories  $\mathbf{R}^{\xi}(t)$  are thus well-approximated according to ab initio DFT MD simulations.

Propagation of the time-dependent electronic wave function is performed for each nuclear trajectory  $\mathbf{R}^{\xi}(t)$  by numerically exact integration (vide infra) of the Time-Dependent Schrödinger Equation (TDSE)

$$\left\{ \frac{\partial}{\partial t} + \frac{i}{\hbar} \mathbf{H}(t) \right\} |\Psi^{\xi}(t)\rangle = 0 \quad (1)$$

Here,  $\mathbf{H}(t)$  is the electronic EH Hamiltonian described in section 2.2., which depends implicitly on time through  $\mathbf{R}^{\xi}(t)$ . Results reported in section 3 are obtained by sampling initial conditions  $\xi$  for nuclear motion, integrating the TDSE over the corresponding ab initio DFT nuclear trajectories, and averaging expectation values over the resulting time-evolved wave functions. Converged results are typically obtained by averaging over fewer than 50 initial conditions, representing the system thermalized under conditions of room temperature and constant volume. However, all results are reported for averages over 100 initial conditions.

The TDSE, introduced by eq 1, is numerically integrated by expanding the time-dependent electron wave function

$$|\Psi^{\xi}(t)\rangle = \sum_q B_q(t) |\phi_q(t)\rangle \quad (2)$$

in the instantaneous eigenstates  $|\phi_q(t)\rangle = \sum_i C_{i,q}(t) |\chi_i(t)\rangle$  of the generalized eigenvalue problem  $\mathbf{H}(t)\mathbf{C}(t) = \mathbf{S}(t)\mathbf{C}(t)\mathbf{E}(t)$ , with eigenvalues  $E_q(t)$ .

The propagation scheme is based on the recursive application of the following short-time approximation:

$$|\Psi^{\xi}(t + \tau/2)\rangle \approx \sum_q B_q(t) e^{-i\hbar E_q(t)\tau/2} |\phi_q(t)\rangle \quad (3)$$

where the evolution of the expansion coefficients

$$B_q(t + \tau) = \sum_p B_p(t) e^{-i\hbar[E_p(t) + E_q(t+\tau)]\tau/2} \times \langle \phi_q(t + \tau) | \phi_p(t) \rangle \quad (4)$$

is approximated as follows

$$B_q(t + \tau) \approx B_q(t) e^{-i\hbar[E_q(t) + E_q(t+\tau)]\tau/2} \quad (5)$$

in the limit of sufficiently thin time slices,  $\tau$ .

The initial electronic state is chosen to correspond closely to the native catechol LUMO or catechol (LUMO+1) of the photoexcited surface complex. Considering that the LUMO and LUMO+1 states of catechol anchoring molecules are important components of the excited electronic states of dyes with high photo-to-current conversion efficiencies (e.g., catechol para-substituted with Ru(II)-polypyridyl complexes), the results presented in sections 3.1. and 3.2. are expected to provide fundamental insight on the effect of temperature on surface charge separation mechanisms in molecular-based photo-optic devices. As discussed in the Introduction, however, the reported results are also relevant to the electron injection dynamics from the native excited states of catechol, even in the presence of competing direct catechol-TiO<sub>2</sub> charge transfer excitations.

The relaxation dynamics is quantitatively described in terms of expectation values of observables computed as  $\langle \hat{A} \rangle = \text{Tr}\{\hat{\rho}(t)\hat{A}\}$ , where  $\hat{\rho}(t)$  is the reduced density operator associated with the electronic degrees of freedom

$$\hat{\rho}(t) = \sum_{\xi} p_{\xi} |\Psi^{\xi}(t)\rangle \langle \Psi^{\xi}(t)| \quad (6)$$

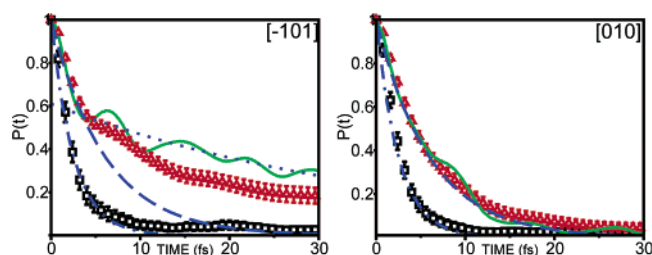


**Figure 4.** Ensemble average adsorbate populations  $\mathbf{P}(t)$  in functionalized catechol/TiO<sub>2</sub> nanostructures extended along the  $[-101]$  (left panel) and  $[010]$  (right panel) crystallographic directions, after instantaneous population of a catechol-LUMO state. The room-temperature electron injection dynamics (black squares) is compared to simulations at 0 K (solid lines); that is, nuclei coordinates are fixed at their fully relaxed configuration, as well as simulations where nuclear positions are fixed in the individual members of the ensemble at their initial room-temperature configurations throughout the injection time (red triangles). Error bars represent the standard deviation resulting from the ensemble average. Broken blue lines are exponential fitting curves characterizing the relaxation times:  $\tau \approx 38$  fs (dotted),  $\tau \approx 6$  fs (dashed), and  $\tau \approx 2.5$  fs (dot-dashed).

with  $p_{\xi}$  the probability of sampling initial conditions, specified by index  $\xi$ , associated with the thermal ensemble of nuclear configurations.

The time-dependent survival probability of an initial electronic state, or transient populations of individual ions, is then determined by computing the time-dependent population  $\mathbf{P}(t)$  as follows:

$$\mathbf{P}(t) = \text{Tr}\{\hat{\rho}(t)\hat{P}_S\} \quad (7)$$

where  $\hat{P}_S$  is the projection operator onto the subset  $S$  of atomic orbitals of interest. In particular, computations of the transient population in the initially photoexcited catechol molecule,  $\mathbf{P}(t)$ , is defined according to eq 7 with

$$\hat{P}_S = \sum_k |\chi_k\rangle \langle S^{-1} \rangle_{jk} \langle \chi_k| \quad (8)$$

where the sum over atomic orbitals includes only atoms of the initially photoexcited catechol adsorbate.

### 3. Results

Results are presented and discussed in three subsections. Section 3.1. presents simulations of electron injection from the catechol LUMO into TiO<sub>2</sub>-anatase nanostructures extended along the  $[-101]$  and  $[010]$  crystallographic directions. Section 3.2. presents analogous results for electron injection from the catechol (LUMO+1). A discussion of the results is presented in section 3.3., with emphasis on the role played by inhomogeneous broadening and nonadiabatic transitions in the underlying relaxation dynamics.

**3.1. Electron Injection from the Catechol-LUMO.** Figure 4 compares the evolution of time-dependent electronic populations, associated with the initially photoexcited surface complex, in functionalized semiconductors at room temperature (squares) and 0 K (solid line). The comparison shows that room-temperature thermal fluctuations significantly speed up the underlying electron injection dynamics. The overall relaxation dynamics at room temperature is largely described by a single exponential decay with a characteristic time  $\tau \approx 2.5$  fs, reaching complete transfer within 10 fs in both functionalized semiconductors extended along the  $[-101]$  and  $[010]$  directions. In contrast, electron injection at low temperature involves a primary charge separation step with a characteristic time  $\tau \approx 6$  fs, followed by slower charge delocalization through the TiO<sub>2</sub>-

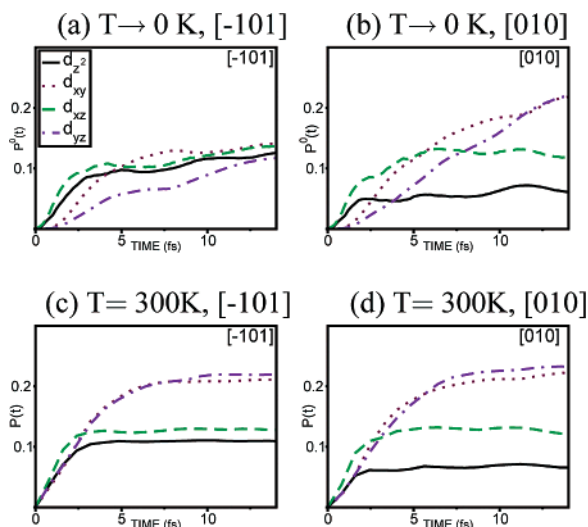


**Figure 5.** Ensemble averaged transient populations of Ti<sup>4+</sup> 3d orbitals constituting the anatase conduction band of nanostructures extended along the  $[-101]$  (left) and  $[010]$  (right) crystallographic directions, at 0 K (top) and room temperature (bottom).

anatase crystal (e.g., a process characterized by a time constant  $\tau \approx 38$  fs in nanostructures extended along the  $[-101]$  direction, as shown in Figure 4, left panel).

Considering that the 10 fs injection time is small compared to the periods of most nuclear vibrations in the functionalized nanostructure (e.g., TiO<sub>2</sub>-anatase normal modes are in the 262–876 cm<sup>-1</sup> range<sup>84</sup>), there is the nontrivial question as to whether thermal nuclear fluctuations speed up the underlying interfacial electron transfer simply by introducing inhomogeneous broadening (i.e., broadening of the distribution of energy levels and electronic couplings), or whether nuclear motion plays a significant role (e.g., inducing additional nonadiabatic transitions). To address this question, Figure 4 also shows results of electron injection considering the effect of inhomogeneous broadening but excluding nonadiabatic effects due to nuclear motion (red triangles). These results are obtained by computing ensemble averaged adsorbate populations, keeping fixed the nuclear positions throughout the whole injection time for each member of the thermal ensemble. The comparison of these results (red triangles) to time-dependent electronic populations obtained at 0 K (solid line) and room temperature (squares) indicates that nuclear motion is most responsible for the underlying speed-up mechanism. It is therefore concluded that, although electronic states are perturbed and mixed in individual members of the thermal ensemble, additional relaxation pathways become active only in the presence of nonadiabatic transitions driven by nuclear motion.

To analyze the molecular origin of the observed speed-up mechanism, Figure 5 presents the decomposition of the electronic population injected in the semiconductor host substrate into individual populations of the Ti<sup>4+</sup>  $d_{xz}$ ,  $d_{z^2}$ ,  $d_{yz}$ , and  $d_{xy}$  orbitals, the main constituent states of the TiO<sub>2</sub> conduction band.<sup>41,92–95</sup> The  $d_{x^2-y^2}$  orbitals are relatively uninvolved in the

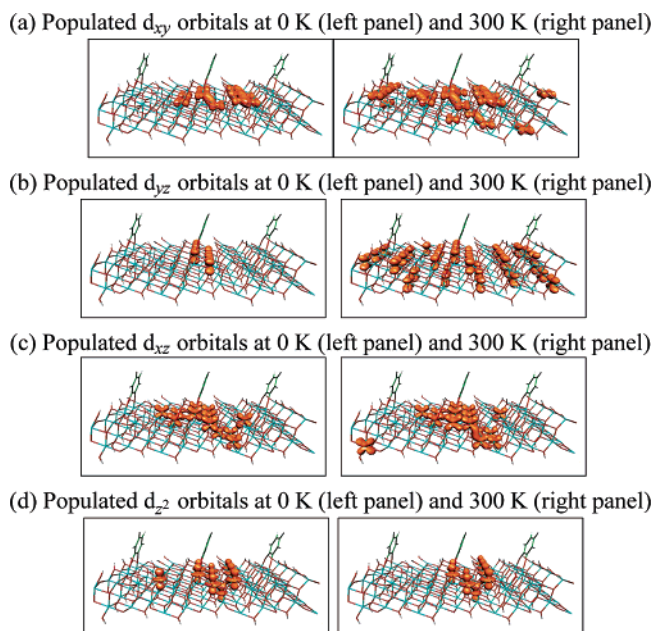


**Figure 6.** Analysis of electronic population at 2.4 fs of dynamics, visualizing the most populated 3d orbitals of Ti<sup>4+</sup> ions at 0 K (left panels) and room temperature (right panels). The global Cartesian coordinate directions corresponding to the orbital labels are:  $\hat{x}$  right along the horizontal frame lines;  $\hat{z}$  down along the vertical frame lines; and  $\hat{y}$  out of the page.

injection process and therefore not considered in the analysis. Figure 5 compares simulations at 0 K (top panels) and room temperature (bottom panels) for nanostructures extended along the  $[-101]$  (left panels) and  $[010]$  (right panels) crystallographic directions.

Figure 5 shows that, at low temperature (upper panels), the early time dynamics is determined by rapid injection into the Ti<sup>4+</sup>  $d_{xz}$  and  $d_{z^2}$  orbitals (acceptor states), followed by an increasing population of the  $d_{yz}$  and  $d_{xy}$  orbitals. Note that the population of the  $d_{yz}$  and  $d_{xy}$  orbitals governs the dynamics at  $t > 5$  fs, as the initially populated  $d_{xz}$  and  $d_{z^2}$  orbitals appear to quickly “saturate” at a certain level of equilibrium population. At room temperature (bottom panels), the rate of population transfer to the  $d_{yz}$  and  $d_{xy}$  is significantly enhanced. This results in an increased rate of delocalization since the  $d_{yz}$  and  $d_{xy}$  states are the primary constituents of delocalized states at the middle and bottom of the conduction band. These results are consistent with a speed-up mechanism based on the enhanced rate of population transfer from acceptor states  $d_{xz}$  and  $d_{z^2}$ , in the vicinity of the photoexcited adsorbate, to the manifold of Ti<sup>4+</sup>  $d_{yz}$  and  $d_{xy}$  states constituting delocalized MOs in the TiO<sub>2</sub> conduction band.

The underlying relaxation mechanism, after photoexcitation of the central catechol adsorbate, becomes evident from a simple population analysis in the STO basis showing the spatial distribution of injected charge associated with the Ti<sup>4+</sup> orbitals comprising the conduction band. Figure 6 presents the detailed distribution of injected charge at a specific time (e.g., 2.4 fs), considering only atomic orbitals with population above a certain cutoff, for nanostructures extended along the  $[-101]$  direction. Instantaneous isodensity surfaces of injected charge projected onto the different Ti<sup>4+</sup> 3d orbitals are shown for nanostructures at 0 K (left panels) and room temperature (right panels). The comparison shows that the net effect of thermal nuclear motion on the underlying electronic relaxation is an enhancement of

(92) Burdett, J. K.; Hughbanks, T.; Miller, G. J.; Richardson, J. W., Jr.; Smith, J. V. *J. Am. Chem. Soc.* **1987**, *109*, 3639–3646.

(93) Mo, S. D.; Ching, W. Y. *Phys. Rev. B* **1995**, *51*, 13023–13032.

(94) Asahi, R.; Taga, Y.; Mannstadt, W.; Freeman, A. J. *Phys. Rev. B* **2000**, *61*, 7459–7465.

(95) Beltrán, A.; Sambrano, J. R.; Calatayud, M.; Sensato, F. R.; Andrés, J. *Surf. Sci.* **2001**, *490*, 116–124.



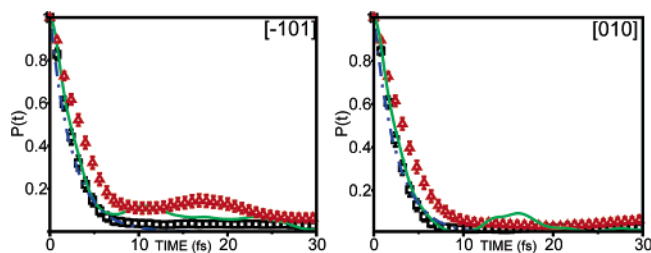


**Figure 7.** Comparison of time-dependent adsorbate populations in functionalized catechol/TiO<sub>2</sub> nanostructures extended along the  $[-101]$  (left panel) and  $[010]$  (right panel) crystallographic directions, after instantaneous population of a catechol-(LUMO+1) state in a surface catechol complex. Black squares represent  $P(t)$ , corresponding to simulations including thermal fluctuations and nuclear motion averaged over 100 initial conditions  $\xi$ . Red triangles depict the analogous ensemble average over simulations conducted with nuclear positions frozen at their initial configurations throughout the injection time. Error bars represent the standard deviation from the thermal ensemble average. The green line corresponds to simulations at 0 K, with nuclear positions frozen at fully relaxed configurations. The dot-dashed blue line is an exponential fitting curve characterizing the relaxation time  $\tau \approx 2.5$  fs (dot-dashed).

delocalization of injected charge among  $d_{xy}$  and  $d_{yz}$  orbitals (panels a and b). In contrast, little difference is observed when comparing the distributions of population among the  $Ti^{4+}$   $d_{xz}$  and  $d_{z^2}$  atomic orbitals at 0 K and room temperature (see Figure 5 panels c and d). These results, which are consistent with Figure 4, show that the underlying speed-up mechanism is based on the enhancement of population transfer from acceptor states localized in the vicinity of the photoexcited adsorbate to delocalized MOs in the host substrate. Analogous results are obtained from the population analysis of nanostructures extended along the  $[010]$  crystallographic direction.

**3.2. Electron Injection from the Catechol (LUMO+1).** This section analyzes the effect of thermal nuclear fluctuations on the electron injection dynamics from the catechol (LUMO+1) state. The comparison of the results presented in this section and the analysis of electron injection from the catechol LUMO, presented in section 3.1., shows that both the electron injection mechanism and the relaxation time scales are sensitive to the spatial symmetry properties of the donor state, even under room-temperature conditions.

Figure 7 shows results of time-dependent adsorbate populations, after instantaneous population of the catechol (LUMO+1) state, in functionalized nanostructures at room temperature (black squares), 0 K (green lines), and simulations that include room-temperature inhomogeneous broadening but exclude nonadiabatic effects due to nuclear motion (red triangles). The exponential fitting curve (blue line), included in Figure 7, defines the characteristic time scale ( $\tau \approx 2.5$  fs) for electron injection.

In contrast to electron injection from the catechol LUMO, the similarity between the injection dynamics at room temperature (black squares) and 0 K (green lines), depicted in Figure 7, indicates that nuclear motion does not significantly affect the time scale for electron injection from the catechol-(LUMO+1). Also in contrast to the injection dynamics from the catechol-LUMO, Figure 7 shows that considering only the effect of inhomogeneous broadening (i.e., without nuclear motion) (red triangles) slows down the underlying interfacial electron transfer dynamics from the catechol-(LUMO+1) state. It is therefore concluded that broadening the distribution of energy levels into nonoptimal states detrimentally affects the

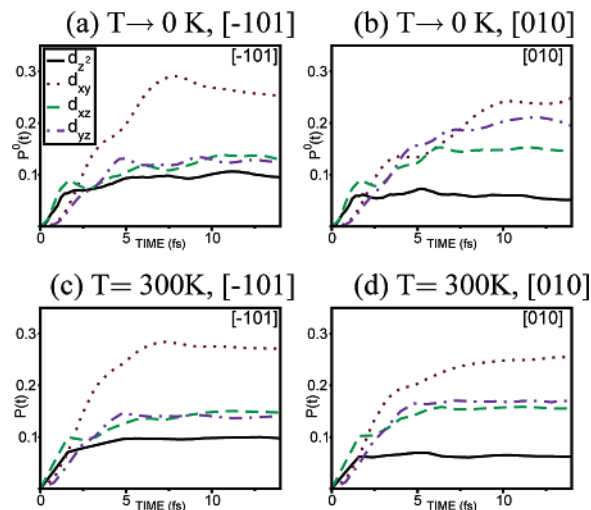


**Figure 8.** Ensemble-averaged transient populations of  $Ti^{4+}$  3d orbitals constituting the anatase conduction band of nanostructures extended along the  $[-101]$  (left) and  $[010]$  (right) crystallographic directions, at 0 K (top) and room temperature (bottom).

strong coupling mechanism of electron injection from the catechol-(LUMO+1).

The comparison of relaxation curves corresponding to room-temperature electron injection from the catechol-(LUMO) and catechol-(LUMO+1) states (see black squares in Figures 4 and 7, respectively) shows that thermal fluctuations give rise to a generic 2.5 fs time scale for injection from either the catechol-LUMO or catechol-(LUMO+1) in nanostructures extended along either the  $[-101]$  or  $[010]$  crystallographic directions.

The similarity in time scales, for room-temperature electron injection from the catechol-(LUMO) and catechol-(LUMO+1), invites the question of whether thermal fluctuations also lead to a correspondingly generic injection mechanism. To address this question, Figure 8 presents the decomposition of electronic population, injected from the catechol-(LUMO+1) state into the populations of the  $Ti^{4+}$  orbitals  $d_{xz}$ ,  $d_{z^2}$ ,  $d_{yz}$ , and  $d_{xy}$ . Simulations at 0 K (top panels) are compared to simulations at room temperature (bottom panels) for semiconductor nanostructures extended along the  $[-101]$  (left panels) and  $[010]$  (right panels) crystallographic directions. Figure 8 shows that thermal nuclear motion does not significantly affect the rate of electron transfer into the different  $Ti^{4+}$  3d orbitals, indicating that the underlying electron injection mechanism is not significantly affected by thermal motion. Moreover, comparing the orbital populations across Figures 5 and 8 supports the general conclusion that the mechanisms for electron injection from the catechol-LUMO and catechol-(LUMO+1) remain significantly different, even at room temperature, although with similar characteristic times.

**3.3. Discussion.** The comparison of time-dependent adsorbate populations, resulting from electron injection dynamics from different initial states and under different conditions (see Figures 4 and 7) indicates that electron injection from catechol-LUMO and LUMO+1 into anatase semiconductors is accelerated by room-temperature thermal fluctuations, proceeding according to ultrafast mechanisms characterized by a single relaxation time  $\tau = 2.5$  fs. The computed time scale is comparable to the sub-3-fs time scale reported by Schnadt et al.<sup>20</sup> for interfacial electron transfer from other excited electronic states (e.g., the LUMO+1 and LUMO+2) of aromatic adsorbates such as (bi)isonicotinic



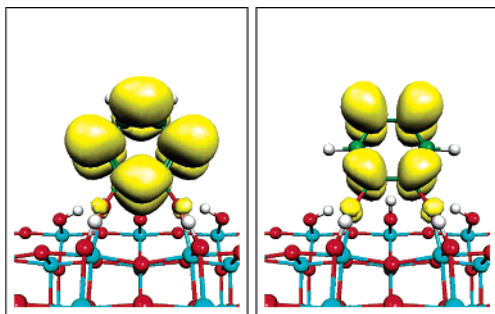


**Figure 9.** Isodensity surface describing the electronic density of the catechol-LUMO (left panel) and catechol-(LUMO+1) (right panel) states.

acid to TiO<sub>2</sub> semiconductors. The analysis of the detailed distribution of injected charge (see Figures 5 and 8) indicates that, although possessing similar characteristic times, electron injection mechanisms remain sensitive to the particular spatial charge distribution of the donor state, even under room-temperature conditions.

Considering the significant amount of research effort reported in recent years, it is important to place the results reported in this paper within the context of related studies.<sup>23,24,33,39–41,46,47</sup> We begin with a comparison to our earlier study of interfacial electron transfer in catechol/anatase semiconductors at low temperature limit.<sup>41</sup> Under such conditions, the differences between injection mechanisms from the catechol-LUMO and LUMO+1 are ultimately attributed to the significantly different character of the LUMO and LUMO+1 states of the catechol adsorbate (see Figure 9). Although both states have an equal number of nodes, the injection mechanism from the catechol-LUMO is mainly “through space” since the injected electron must tunnel from the catechol-LUMO to the hexacoordinated Ti<sup>4+</sup> ion (see Ti(6) ion in Figure 2) due to the lack of conjugated  $\pi$  system electron density near the linking oxygen atoms (see Figure 4). The Ti<sup>4+</sup> ion thus becomes a bottleneck for charge injection in nanostructures extended along the  $[-101]$  direction. In contrast, injection from the catechol-(LUMO+1), in which a nodal plane in the electron density bisects the catechol molecule (see Figure 7), proceeds through chemical bonds associated with the two pentacoordinated Ti<sup>4+</sup> ions directly anchoring the adsorbate (see Ti(5) ions in Figure 2) and quickly delocalizes along the  $[010]$  crystallographic direction on the surface of the TiO<sub>2</sub>-anatase, before separating from the surface by delocalization along the  $[101]$  direction (i.e., further into the semiconductor).

The results reported in this paper indicates that inhomogeneous broadening partially breaks the nodal symmetry of the donor state, slightly mixing the two injection pathways. However, such a perturbation only marginally alters the underlying mechanism and time scales, as shown in Figures 4 and 7, slightly speeding up or slowing down the transfer process. However, room-temperature thermal fluctuations enhance non-adiabatic processes between those MOs involved in the primary injection process (composed of the  $d_{xz}$  and  $d_z^2$  AOs of Ti<sup>4+</sup>) and those responsible for electronic delocalization (composed of the  $d_{yz}$  and  $d_{xy}$  AOs of Ti<sup>4+</sup>). Therefore, the resulting effect on electron injection from the catechol-LUMO is a net speed up of interfacial electron transfer since the acceptor state in the hexacoordinated Ti<sup>4+</sup> ion is no longer a bottleneck for charge injection, as it is at low temperature. In contrast, injection from the LUMO+1, relying primarily on a “through-bond” mecha-

nism with rapid delocalization, is not so significantly affected by thermal fluctuations.

The main conclusion suggested by the analysis of distribution of injected charge, shown in Figures 4–8, is that thermal nuclear motion is largely responsible for speeding up the electron injection mechanism in the presence of inhomogeneous broadening. These effects serve to accelerate the overall interfacial electron transfer process without affecting the dependence of the underlying mechanism on the particular symmetry properties of the photoexcited state in the donor adsorbate molecule.

We continue with a comparison to a valuable series of recent theoretical studies, based on the Anderson–Newns Hamiltonian, including a description of dye–semiconductor electron transfer due to Ramakrishna, Willig, and May<sup>46,47</sup> and recent work by Thoss, Kondov and Wang<sup>40</sup> on the behavior of similar models. Both studies involve general theoretical treatments of a single electronic donor state coupled to a quasi-continuum of semiconductor acceptor states, with coupling to a bath of quantum harmonic oscillators.

The study of Ramakrishna and co-workers indicates that electron transfer from an excited dye state is essentially independent of vibrational modes, under conditions of either constant (strong) electronic coupling between donor and acceptor in the wide-band limit or in the zero-reorganization energy limit. In this fastest case, electronic injection will be independent of temperature and will not be modulated by vibrational wave packet motion. It is judged within this study that a temperature dependence of injection will, however, be observable in most realistic systems, where the density of states or the electronic coupling between donor and acceptor states varies significantly. Therefore, injection rates computations based solely on electronic coupling are expected to be overestimated.

The study of Thoss, Wang and co-workers presents a similar analysis, concluding that in cases where vibrational degrees of freedom have a significant effect on the electronic dynamics nuclear wave packets will modulate the electronic injection, often leading to slower or incomplete injection. These results are consistent with electron injection occurring much faster than vibrational relaxation. This analysis is therefore consistent with previous experimental studies, reporting the footprint of nuclear wave packet motion on electron injection in other functionalized TiO<sub>2</sub> semiconductors.<sup>23,24</sup>

As pointed out by Thoss, Wang and co-workers,<sup>40</sup> these related theoretical studies are expected to be most relevant to systems where the donor state is energetically situated close to the bottom of the conduction band, where the electronic coupling between adsorbate and semiconductor is weak, or where the system is prepared significantly displaced from the equilibrium geometry of the donor state. It is therefore important to note that such conditions are partially incompatible with the catechol/TiO<sub>2</sub>-anatase system, where donor states are energetically embedded in the TiO<sub>2</sub> conduction band and strongly coupled to the semiconductor acceptor states. Furthermore, the donor adsorbates are prepared close to their nuclear equilibrium geometries since the equilibrium positions and vibrational frequencies are only slightly affected by photoexcitation to bound excited states (e.g., HOMO–LUMO excitations).<sup>57</sup>

The treatment of electronic relaxation, presented in this paper, implicitly assumes negligible reorganization energy  $\lambda$  of the surface complex during the injection time. This approximation

is consistent with the wide-band limit, implying that  $\lambda$  is small relative to the width of the conduction band (i.e.,  $\lambda \ll 5$  eV) and agrees with the fact that the internal reorganization energies associated with aromatic organic molecules are typically of the order of a tenth of an electron Volt. However, in contrast to the general formulations, we compute the electronic structure at the atomistic level, allowing for an explicit description of the density of states and electronic couplings. Thus it is not by design that our simulations explore the strong coupling limit, but rather as a characterization of the electronic structure of the catechol/anatase system. The explicit treatment of electronic couplings also allows one to investigate aspects that might be beyond the limitations of model systems, including the detailed molecular origin of the speed up mechanism. This process is attributed to nonadiabatic transitions between acceptor states in the vicinity of the molecular adsorbate and states delocalized throughout the host substrate. The explicit atomistic model also allows one to predict a minimal effect of nuclear dynamics on the primary electron transfer event that populates acceptor states in the vicinity of the photoexcited adsorbate since high injection rates are predicted for catechol/anatase systems even under low temperature conditions. The explicit atomistic simulations also suggest that the experimental detection of a vibrational imprint on the underlying electronic dynamics would be unlikely in the catechol/TiO<sub>2</sub> system since the overall injection is completed within 10 fs under room-temperature conditions.

Finally, it is important to compare the results reported in this paper with a recent series of studies by Prezhdo and co-workers,<sup>33,37,39</sup> reporting a thermal nuclear motion component to the electron injection rates of interfacial electron transfer in alizarin/rutile semiconductors. The mechanism by which nuclear thermal fluctuations speed up the overall electron injection dynamics in that system, however, seems to be significantly different from the catalytic effect of nuclear motion in catechol/anatase semiconductors. This is not surprising, however, since the donor states in the alizarin/rutile system are off-resonance relative to the conduction band. Nuclear motion opens previously forbidden electron injection channels by bringing these off-resonant donor states of alizarin surface complexes in resonance with the conduction band. In contrast, the donor states of catechol surface complexes are already in resonance with the manifold of electronic states in the TiO<sub>2</sub> conduction band, analogously to dye surface complexes with high photo-to-current conversion efficiencies (e.g., catechol para-substituted with Ru(II)-polypyridyl complexes). The speed-up mechanism reported for catechol/anatase semiconductors herein, while different from the alizarin/rutile interface, should be particularly relevant to the understanding of temperature effects on surface charge separation mechanisms in typical molecular-based photo-optic devices, especially considering that photovoltaic devices usually involve donor adsorbate states in resonance with acceptor states in the semiconductor conduction band.

#### 4. Conclusions

In this paper, we have shown that room-temperature nuclear fluctuations significantly affect the interfacial electron transfer

dynamics in TiO<sub>2</sub>-anatase semiconductors functionalized with catechol. Our results are noteworthy since catechol is a prototype of aromatic anchoring ligands upon which a wide range of molecular structures can be attached for specific functionalities. This work has been accomplished by implementing a methodology developed in previous work,<sup>41–43</sup> combining ab initio DFT molecular dynamics simulations and quantum dynamics propagation of transient electronic excitations based on a time-dependent extended Hückel model Hamiltonian.

We have shown that interfacial electron transfer in catechol/TiO<sub>2</sub> at room temperature can be described by a single exponential decay, with a characteristic time  $\tau \approx 2.5$  fs that quantitatively describes the relaxation of electronic population in the initially photoexcited catechol adsorbate. In addition, it is reported that thermal fluctuations reduce the anisotropic character of charge diffusion along different directions in the anatase crystal and make similar the electron injection rates from adsorbate states of different spatial charge distribution. It is also shown that, despite this apparent homogenization of the time scales of injection, the interfacial electron transfer mechanisms from electronic states of different character remain distinct even in the presence of room-temperature thermal fluctuations. These results complement and contrast earlier studies of electron injection under cryogenic temperature conditions<sup>41</sup> and lend support to the interpretation of experimental data suggesting ultrafast (sub-10-fs) electron injection in similarly strongly coupled semiconductor–dye systems.<sup>19–21</sup> The longer time behavior of the injected electron in large systems, and its possible correlation with the hole in the adsorbate monolayer, is a subject of current study.

We have shown that, in contrast to the influence of nuclear motion on the interfacial electron transfer in other functionalized semiconductors, the catechol/anatase system involves donor states embedded in the conduction band of the host substrate. Therefore, thermal nuclear fluctuations simply speed up the interfacial electron transfer by creating additional nonadiabatic relaxation pathways between electron acceptor states, localized in the vicinity of the adsorbate, and delocalized states extended throughout the semiconductor material.

**Acknowledgment.** V.S.B. acknowledges supercomputer time from the National Energy Research Scientific Computing (NERSC) Center and financial support from Research Corporation, Research Innovation Award # RI0702, a Petroleum Research Fund Award from the American Chemical Society PRF # 37789-G6, a junior faculty award from the F. Warren Hellman Family, the National Science Foundation (NSF) Career Program Award CHE # 0345984, the NSF Nanoscale Exploratory Research (NER) Award ECS # 0404191, the Alfred P. Sloan Fellowship (2005-2006) from the Sloan Foundation, a Camille Dreyfus Teacher-Scholar Award for 2005, a Yale Junior Faculty Fellowship in the Natural Sciences (2005), and start-up package funds from the Provost's office at Yale University.

JA055185U